International Journal of Impact Engineering 112 (2018) 180–192

Contents lists available at ScienceDirect

International Journal of Impact Engineering

journal homepage: www.elsevier.com/locate/ijimpeng

Johnson-Cook parameter evaluation from ballistic impact data via iterative FEM modelling

M Burley, JE Campbell, J Dean, TW Clyne*

Department of Materials Science & Metallurgy, Cambridge University, 27 Charles Babbage Road, Cambridge CB3 0FS, UK

ARTICLE INFO

Keywords:
Indentation
High strain rates
Impact indentation
Finite element analysis
Plasticity

ABSTRACT

A methodology is presented for evaluating a strain rate sensitivity parameter for plastic deformation of bulk metallic materials. It involves ballistic impact with a hard spherical projectile, followed by repeated FEM modelling, with predicted outcomes (displacement-time plots and/or residual indent shapes) being systematically compared with experiment. The "correct" parameter value is found by seeking to maximise the value of a "goodness of fit" parameter (g) characterizing the agreement between experimental and predicted outcomes. Input for the FEM model includes data characterizing the (temperature-dependent) quasi-static plasticity. Since the strain rate sensitivity is characterised by a single parameter value (C in the Johnson–Cook formulation), convergence on its optimum value is straightforward, although a parameter characterizing interfacial friction is also required. Using experimental data from (both work-hardened and annealed) copper samples, this procedure has been carried out and best-fit values of C ($\sim$0.016 and $\sim$0.030) have been obtained. The strain rates operative during these experiments were $\sim 10^4$–$10^6\ s^{-1}$. Software packages allowing automated extraction of such values from sets of experimental data are currently under development.

1. Introduction

It is well known that metals exhibit strain rate-dependent plastic flow behaviour. The mechanisms responsible for this sensitivity (related to dislocation mobility and alternative deformation modes) are known, but it cannot be predicted in any fundamental way and it is not easy to capture experimentally (for high strain rates). Nevertheless, simulation of this strain rate dependence is essential for FEM modelling [1] of many situations involving high strain rates (ballistics, explosions, crashes, machining, cutting etc). Since such modelling is routinely carried out on a massive global scale, often with little scope for cross-checking of its reliability, validation of the procedures, and accurate quantification of the characteristics for a range of materials, are very important.

In order to implement such modelling, appropriate constitutive relations, and the values of parameters in them, are required. The most commonly-used expression, particularly for use in FEM models, is that of Johnson and Cook [2], which is often written in the form

$$\sigma = \{\sigma_Y + K\varepsilon_p^n\}\left[1 - \left(\frac{T - T_0}{T_m - T_0}\right)\right]\left(1 + C\ln\left\{\left(\frac{d\varepsilon_p}{dt}\right)/\left(\frac{d\varepsilon_p}{dt}\right)\right\}\right). \quad (1)$$

where σ_Y is the yield stress, K is the strain hardening coefficient, n is the strain hardening exponent, T_m is the melting temperature, T_0 is a reference (ambient) temperature, m is the temperature coefficient, ($d\varepsilon_p/dt$) is the (plastic) strain rate, $(d\varepsilon_p/dt)_0$ is a reference (quasi-static) strain rate and C is the strain rate sensitivity parameter. (A complete nomenclature listing is provided in Appendix A). The first term (sometimes called the Ludwik–Hollomon, L-H, equation) thus dictates the quasi-static yielding and work hardening behaviour, the second the temperature dependence and the third the strain rate sensitivity. This last term includes the logarithm of the strain rate, normalised by a reference value. Apart from this normalizing strain rate, usually taken to be a quasi-static rate, only the value of C is required in order to characterise the strain rate sensitivity. It should be noted, however, that the temperature dependence is often significant, since the imposition of rapid plastic straining is likely to cause local temperature rises, with most of the plastic work normally being released as heat.

It may, however, be noted that, for purposes of establishing the value of the strain rate sensitivity parameter, C, it's not essential to use an analytical expression for the first term in Eq. (1). Since this $\sigma(\varepsilon)$ relationship is taken to be fixed, an experimentally-obtained set of data pairs can be employed, instead of a functional relationship. This is done in the present work, since it turned out to be difficult to represent the (quasi-static) plasticity accurately with an analytical expression.

Eq. (1) is considered to provide a fairly realistic representation of the behaviour, at least in the regime below that in which shock waves [3] are likely to have a significant effect (ie it should be reliable for sub-

* Corresponding author.
E-mail address: twc10@cam.ac.uk (T. Clyne).

https://doi.org/10.1016/j.ijimpeng.2017.10.012
Received 15 September 2017; Received in revised form 24 October 2017; Accepted 27 October 2017
Available online 07 November 2017

sonic impact velocities). Several minor variations to the Johnson–Cook (J-C) formulation have been put forward [4–6], but the basic form is in general considered to be quite reliable. It should nevertheless be recognised that it is essentially just an empirical expression, and also that several other formulations have been proposed. There have certainly been criticisms [7] of the J-C formulation. Moreover, a recent investigation [8] has covered the effect of the exact shape of the yield envelope, in a study oriented towards FEM simulation of ballistic impact.

Conventional mechanical testing procedures have certain limitations for this purpose and the maximum strain rates achievable in a controlled way during uniaxial tensile or compression testing are below those that are often of interest. Jordan et al. [9] reported on such testing carried out at strain rates of up to 10^4 s^{-1}, although displacements were measured on the cross-head and are unlikely to have been very accurate at such high strain rates. These authors tested as-received and annealed copper samples, reporting that an increase in the strain rate by a factor of 10^6 raised the flow stress by factors of ~30% and 100% respectively (corresponding to values of C in the J-C formulation of ~0.02 and 0.07). These values may not be very reliable, although it is plausible that softer (annealed) material may be more susceptible to strain rate hardening.

In practice, the split Hopkinson bar (SHB) test [10,11] is commonly employed, and can create relatively high strain rates (~10^3–10^5 s^{-1}), although it is subject to significant levels of uncertainty, arising from various sources [12,13]. There is also the Taylor cylinder test [14–16], although this is similar in concept to the SHB test and subject to the same type of limitations. Despite these issues, there have been many publications reporting on outcomes of testing of this type, often involving evaluation of C. Values obtained in this way include 0.001 for a 1000 series Al alloy [17], 0.023 for a 7000 series Al alloy [18], 0.039 for an AISI-1018 low carbon steel and 0.011 for an AISI-4340 low alloy steel [19], 0.048 for an AISI-1018 low carbon steel [20] and 0.009 for an ultra-fine grained copper [21]. It's difficult to rationalise such outcomes in any way and even this small cross-section of results indicates that they are not always consistent. Nevertheless, it's clear that some metals exhibit considerably greater strain rate sensitivity than others.

There have been many publications involving use of FEM for simulation of impact testing procedures, with the objective of investigating the strain rate sensitivity of the material. These include FEM studies [15,19,20,22] of the SHB and similar types of test. Furthermore, several studies [23–25] have involved FEM simulation of the impact of a sharp indenter to explore the strain rate dependence of the yield stress. However, none of these studies has treated the evolving stress and strain fields in detail, many do not take account of temperature changes during the test and few involve any systematic iterative FEM: the focus has tended to be on effective average strain rates during tests.

Nevertheless, the inverse FEM method (ie. iterative FEM simulation of a particular test procedure, initially using trial input parameter values and then modifying them so as to obtain optimal agreement with experimental outcomes) is a potentially powerful technique. Its application to ballistic indentation is particularly attractive, since a wide range of local strain rates can be generated and there are few uncertainties in the formulation of the model (as a free body problem). Furthermore, the requirements in terms of sample dimensions and preparation procedures are less demanding. It is also potentially easier than SHB-type tests in terms of experimental implementation (provided that suitable arrangements for monitoring of experimental outcomes can be employed).

One of the challenges in implementing iterative FEM procedures concerns the methodology for converging on an optimied set of parameter values. With multiple parameters, this can be complex, although it's clear that the “goodness-of-fit” between modelled and experimental outcomes should be quantified and progress has been made [26] on systematic optimization of this for instrumented indentation with spheres, aimed at characterizing quasi-static plasticity (via three parameter values). It can be seen from Eq. (1) that, when employing the J-C constitutive law, only one parameter (C) needs to be evaluated, provided that the quasi-static plasticity parameters (or a set of data pairs) have already been obtained. This simplifies the convergence procedure considerably. An overall methodology is proposed in the current work and illustrated via its implementation for two different materials, using two outcomes (displacement history of the projectile and residual indent shape) for the optimization procedure.

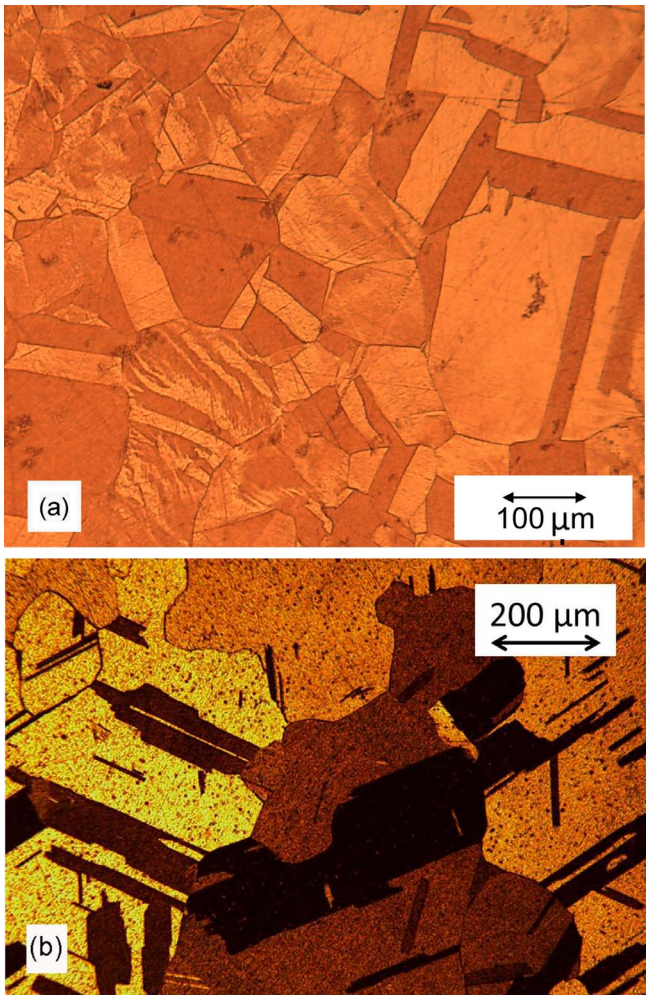

Fig. 1. Optical micrographs of transverse sections of the extruded copper (a) as-received (b) after annealing.

2. Experimental procedures

2.1. Materials and microstructures

Two materials were employed in the present investigation. An extruded (25 mm diameter) OFHC copper bar was used both in the as-received state and after an annealing treatment of 2 h at 800 °C, in an inert atmosphere. This treatment caused recrystallization and hence a substantial drop in the hardness of the material. Both conventional uniaxial compression testing and dynamic (ballistic) indentation were carried out on both materials, along the extrusion axis. The grain structures (in transverse section) are shown in Fig. 1. It can be seen that the grain size was of the order of 30–50 µm in the as-received material, but had coarsened to about 300–400 µm after annealing (which stimulated recrystallization). Some annealing twins are also present.

Such (relatively coarse) grain structures, which are far from uncommon, present challenges in terms of using indentation to obtain

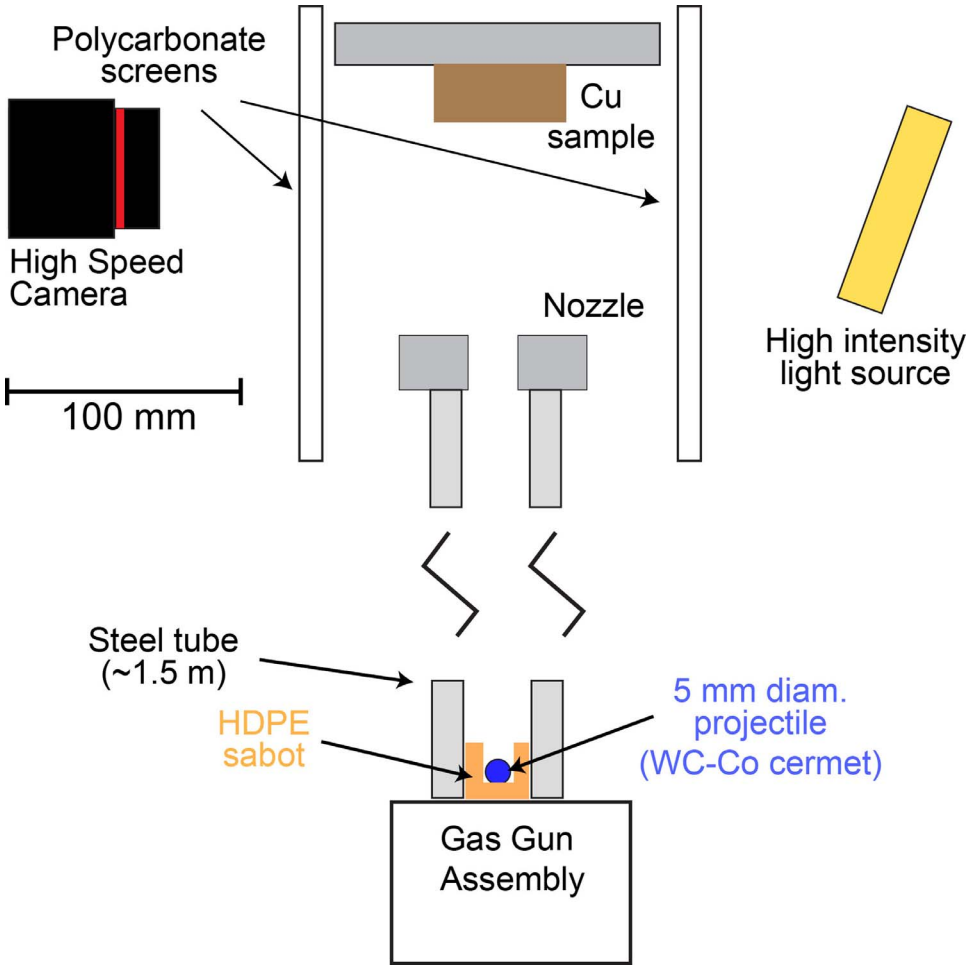

Fig. 2. Schematic depiction of the gas gun set-up for ballistic indentation.

(bulk) properties, since it's clear that these can only be obtained by mechanically interrogating a representative (multi-grain) volume. The indents were therefore created using relatively large cermet (WC-Co) spheres (of diameter 5 mm), obtained from Bearing Warehouse Ltd (who also supplied a datasheet giving their elastic properties). The resultant indent size depends, of course, on both the impact velocity and the sample hardness, but in general they were of the order of 1 mm in diameter (and were larger for the softer material, which had the larger grain size), so multi-grain volumes were being tested in all cases. Of course, projectiles in this size range are common, and much smaller ones would have been difficult to use, but (quasi-static) instrumented indentation is frequently carried out on a much finer scale than this.

For present purposes, it's important to be able to simulate the stress-strain curve over a wide range of strain (perhaps up to 200% or more, depending on the depth of projectile penetration). This is well beyond the levels to which conventional uniaxial testing can be carried out (since necking/failure tends to occur in tension and barrelling in compression). This is not such a problem for the as-received (work-hardened) material, since the rate of further work hardening is low and the flow stress will tend to remain approximately constant up to large strains. For the annealed material, however, the initial work hardening rate is high and extrapolating this behaviour to strains beyond the measurable regime (typically only up to about 20–25%) is subject to considerable error. This problem was tackled by applying three swaging operations to the annealed material, each inducing a well-defined level of (true) plastic strain, extending up to about 200%. These materials were tested in compression (see below) and the yield stress taken as a flow stress level for the annealed material at the strain concerned. This allowed the stress-strain curve to be simulated (as a set of data pairs) over the complete strain range of interest.

2.2. Uniaxial compression testing

In order to obtain the “correct” (quasi-static) plasticity parameter values for these two materials, samples were subjected to uniaxial compression testing between rigid (hardened steel) platens. Cylindrical specimens (6 mm height, 5 mm diameter) were tested at room temperature (22 °C ± 2 °C), using MoS_2 lubricant to minimise barrelling. Displacements were measured using an eddy current gauge, with a resolution of about 25 μm. Testing was carried out under displacement control (at a rate of 2 mm min^{-1}), using an Instron 5562 screw-driven testing machine, with a load cell having a capacity of 30 kN. The strain rate generated during these tests, which was taken to be the reference (quasi-static) rate for use in Eq. (1), was thus about 5.5 10^{-3} s^{-1}.

Tests were done up to displacements of about 1.5 mm (25% nominal plastic strain), so that each test took about 45 s to complete. It was confirmed that barrelling was negligible over this strain range. Tests were carried out over a range of temperature, up to 300 °C. (It was confirmed by FEM modelling - see §5 – that temperatures reached during ballistic impact were lower than this, except possibly for very short transients in a thin surface layer.)

Several repeat tests were carried out. Both stress and strain levels were converted from nominal to true values, using the standard expressions:

$$\sigma_T = \sigma_N(1 + \varepsilon_N), \qquad \varepsilon_T = \ln(1 + \varepsilon_N) \tag{2}$$

with the strains in this case being negative (compressive), so that the true stress has a magnitude lower than the nominal value, while the

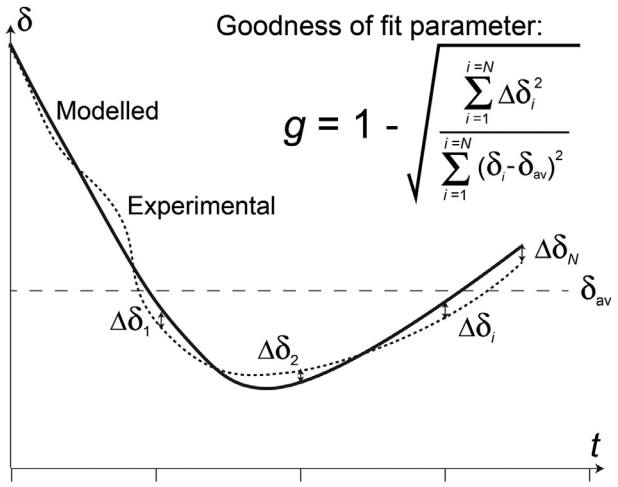

Fig. 3. Schematic of an experimental displacement-time plot, with a modelled prediction superimposed, and the definition of the goodness-of-fit parameter, *g*.

true strain has a larger magnitude than the nominal strain. In order to explore the possibility of (plastic) anisotropy of the material, testing was carried out on samples having the loading axis transverse to the extrusion axis of the rod (ie in the radial direction), as well as along this axis.

2.3. Ballistic impact

2.3.1. Gas gun

The set-up employed is depicted in Fig. 2. The gas gun used is based on three coaxial components - a 2 m barrel and two high-pressure chambers. The barrel is separated from one high-pressure chamber by a thin Cu membrane (several tens of microns in thickness), with a similar membrane between it and a second chamber. Both chambers are filled with nitrogen, with pressure drops between barrel and first pressure chamber, and between the two pressure chambers, both set to values (just) insufficient to burst the membranes. The first chamber is then evacuated, creating pressure differences across both membranes that are sufficient to cause bursting. The expanding gas then drives the projectile, held inside an HDPE sabot, along the barrel of the gun. At the end of the barrel the sabot is stripped from the projectile by a "sabot stripper", so that only the projectile (a 5 mm diameter WC-Co cermet ball) strikes the sample. The impact velocity is controlled, at least approximately, via manipulation of the thickness of the membranes and the pressure in the chambers. All impacts were at normal incidence, with samples rigidly supported at the rear, employing impact speeds in the range 50–300 m s^{-1}. The samples were obtained from the copper rods by machining into cylinders of diameter 25 mm and height 30 mm.

It may be noted that it was found to be important to secure the sample rigidly on its rear surface. The modelling covered everything happening within the sample, but one of the boundary conditions was that it was supported on an immoveable surface and it was important to ensure that this condition was closely approached in practice. A massive, rigidly-held steel plate was used to provide this support.

2.3.2. High speed photography

A Phantom V12.1 high-speed camera was used to record impact events, with a time resolution of ~1.4 μs (frame rate of 717,948 s^{-1}) and exposure time of 0.285 μs. (There was thus a dead-time between exposures of about 1.1 μs: this was done deliberately, in order to obtain a combination of minimal blurring of individual images and data capture over a relatively long period, within the memory limit of the camera). Linear spatial resolution of ~50 μm per pixel was achieved and images comprised 128 × 24 pixels. From video sequences and known calibration factors, time-displacement histories were then extracted for the projectile motion, with attention being focussed on the location of the rear of the projectile.

2.3.3. Residual indent topography

A Taylor Hobson (Talysurf) profilometer (ie a contacting stylus), with a wide-range inductive gauge and 20 μm radius cone recess tip, was used to measure residual indent profiles. Scans were carried out in two perpendicular directions, both through the central axis of the indent (found by carrying out several closely-spaced parallel scans). The height resolution of these scans is about 25 μm. Tilt correction functions were applied to the raw data, based on the far-field parts of the scan being parallel. The average profile from the two orthogonal scans was used in the *g*-screening exercise.

2.4. Goodness of fit Parameter, g

Central to this methodology is the definition of a "goodness of fit" parameter, *g*, characterizing the level of agreement between predicted and measured outcomes. The definitions employed here (for displacement-time and displacement-radius plots) are:

$$g = 1 - \sqrt{\frac{\sum_{i=1}^{N} \Delta\delta_i^2}{\sum_{i=1}^{N} (\delta_i - \delta_{av})^2}} \tag{3}$$

with the meanings of the parameter values being illustrated (for a displacement-time plot) in Fig. 3, and also defined in the nomenclature listing. For the displacement-time data, values of δ were compared at time intervals of the order of 1.4 μs. For the residual indent shape, displacement (height) differences were evaluated at *r* intervals of about 100 μm. The total number of points at which comparisons were made (*N*) was respectively 30 and 50 for displacement-time data from as-received and annealed samples. (These values of *N* were chosen to ensure similar weighting was given to the penetration and rebounding parts of the motion.) For the residual indent shape data, $N = 50$ was used for both samples. It can be seen from the form of Eq.(3) that perfect agreement between the two sets of data (eg. $\Delta\delta_i = 0$ for all i values) gives a value for *g* of 1, while no agreement (ie predictions random about the average value) leads to a value of 0.

3. FEM modelling

3.1. Model formulation

An axi-symmetric FEM model for simulation of impact and rebound was built within the Abaqus package. Both projectile and target were modelled as deformable bodies and meshed with first order quadrilateral and/or triangular elements. The projectile is expected to remain elastic throughout, although it can be important in high precision work of this nature not to treat it as a rigid body: not only is it possible for its elastic deformation to make a significant contribution to the overall displacement, but its lateral Poisson expansion could affect the outcome, particularly if attention is being focused on the shape of the residual impression. Of course, such modelling also allows a check to be made on whether there is any danger of the projectile being plastically deformed.

The volume elements in the model were CAX4RT types (linear coupled temperature-displacement), with about 5000 elements in the sample and about 2000 in the projectile. Meshes were refined in regions of the sample close to the indenter. Sensitivity analyses confirmed that the meshes employed were sufficiently fine to achieve convergence, numerical stability and mesh-independent results. The complete sample was included in the simulation, with its rear surface rigidly fixed in place. In modelling the complete sample, contributions to the displacement caused by its elastic deformation (as well as plastic deformation) are fully captured. A typical set of meshes is shown in Fig. 4.

Simulation required specification of an initial velocity for the

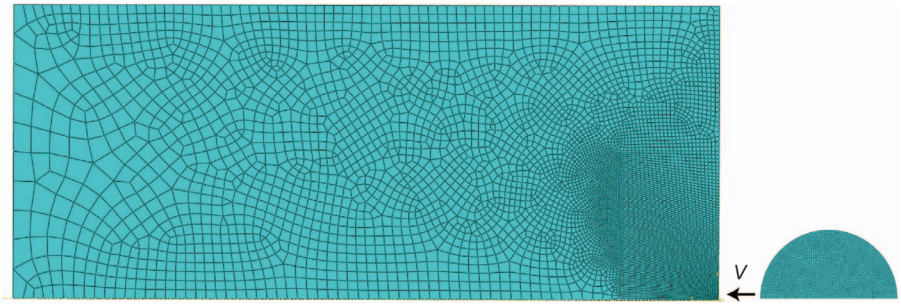

Fig. 4. Typical mesh configurations for the FEM modelling.

projectile, after which it moved in free flight to strike the sample at normal incidence. Any effects of air resistance between sample and projectile were neglected. Displacements of the projectile were output at a series of specified time values (~1.4 μs intervals) throughout penetration and immediately after rebound (covering a period of the order of 40 μs). The residual indent shape, and the surrounding fields of residual stress, plastic strain, strain rate and temperature were also predicted in each case.

All material properties were assumed to be isotropic. The Young's moduli, E, and Poisson ratios, ν, of projectile and sample were respectively taken to be 650 GPa and 0.21 (cermet) and 120 GPa and 0.30 (copper). The density of the cermet was measured to be 14,800 kg m^{-3}. The thermal conductivity, κ, of the copper was taken (from the literature) to be 401 W m^{-1} K^{-1} and its heat capacity, c, to be 3.45 MJ m^{-3} K^{-1}. The fraction of the plastic work converted to heat (Taylor–Quinney coefficient) was set at 95%. (Slightly different values are sometimes used, but there is in any event no solid theoretical basis on which to estimate it - the underlying idea is that the remaining energy goes mainly into the creation of new dislocations, so the value could be higher for a material that is already work-hardened, but it is not really viable to attempt any prediction.) Heat transfer from sample to projectile was neglected. The plasticity properties of the sample were simulated using the J-C constitutive relation (Eq. (1)), with the first term represented by a set of data pairs - see §4.

There is also the issue of the nature of the frictional contact between projectile and sample during the penetration. The standard representation of this effect (within Abaqus) is to ascribe a coefficient of friction, μ, to the interfacial contact, such that sliding between the two surfaces requires a shear stress, τ, given by

$$\tau = -\mu\sigma_n \tag{4}$$

where σ_n is the normal stress at the interface. The value of μ is clearly expected to depend on the surface roughness (of projectile and sample), and possibly on other factors, and so cannot be predicted *a priori*. In the present work, it was regarded as a variable to be adjusted to give optimal levels of agreement, particularly regarding the residual indent shape, which is expected to be sensitive to the value. In general, however, since both surfaces are smooth, a relatively low value ($< \sim 0.2$) is expected to be appropriate.

As with any FEM implementation of a constitutive law in the form of a family of curves, a rationale is required concerning the progressive deformation of individual volume elements. As the projectile penetrates, any particular element in the sample will experience changes in both temperature and strain rate. At any stage during the process, the values of these two in the location concerned will define the appropriate stress-strain curve for deformation during the next time interval. In the current work, it has been assumed that the cumulative (von Mises) strain defines the 'state' of (a volume element of) the material. This then fixes the point on the appropriate stress-strain curve where the gradient is to be evaluated. (This gradient defines what will now occur - ie determines the increase in flow stress needed to generate an imposed strain increment or, equivalently, determines how much straining will result from the availability of an increment of flow stress.) By using the von Mises stress and strain in an expression based on uniaxial (quasi-static) testing, the von Mises yielding criterion is implicitly being used to predict the onset of plasticity. This is common, although the effect of varying this criterion between von Mises and Tresca limits has been explored in the recent paper by Holmen et al [8].

An investigation has also been made into how the plastic work is distributed in terms of the strain rate during the deformation. After each increment of time, for each volume element, the stress, incremental strain and strain rate are recorded. The work done during that time interval is evaluated (= stress × strain × volume) and that increment of work is associated with the strain rate concerned. Expressed mathematically, the increment of work done in the jth volume element during the kth time increment is

$$\Delta W_{j,k} = \sigma_{j,k}\Delta\varepsilon_{j,k}v_j \tag{4a}$$

Clearly, the work done during the kth time increment is given by

$$\Delta W_k = \sum_{j=1}^{j=M} \Delta W_{j,k} \tag{5}$$

where the summation is over the total number (M) of volume elements, and the total work done is

$$W_{tot} = \sum_{k=1}^{k=S} \Delta W_k \tag{6}$$

with this summation being over the total number (S) of time increments. The total strain rate range is divided into a number of sub-ranges (bins) and the work done within each range is then evaluated after a binning operation. This can be expressed as

$$W_{bin,p} = \sum_{k=1}^{k=S} \sum_{j=1}^{j=M} (\Delta W_{j,k} f_{j,k,p}) \tag{7}$$

where $f_{j,k,p}$ is a function ascribed a value of 1 or 0, depending on whether the strain rate associated with the increment of work $\Delta W_{j,k}$ does or does not fall within the range of the pth bin.

3.2. JC parameter evaluation

There is effectively only a single material property parameter (C) to evaluate, so the operation of converging on an optimal solution is relatively straightforward. However, there is the issue of the coefficient of friction, which, realistically, cannot be obtained via any separate experimental study and so has to be treated as another parameter to be iteratively optimised. In the present work, however, the effect of these two parameters (C and μ) was decoupled, so that optimization was carried out first for μ, using a fixed value of C, and then vice versa. This process was repeated a couple of times. Since two experimental outcomes ($\delta(t)$ and $\delta(R)$ plots) are being studied, there is scope for a more systematic convergence operation, simultaneously incorporating both C and μ, but it was not considered necessary for present purposes. It may be noted at this point that, while repeated FEM simulation is integral to the procedure being used, there are good prospects for this to be integrated into user-friendly automated software packages. This is

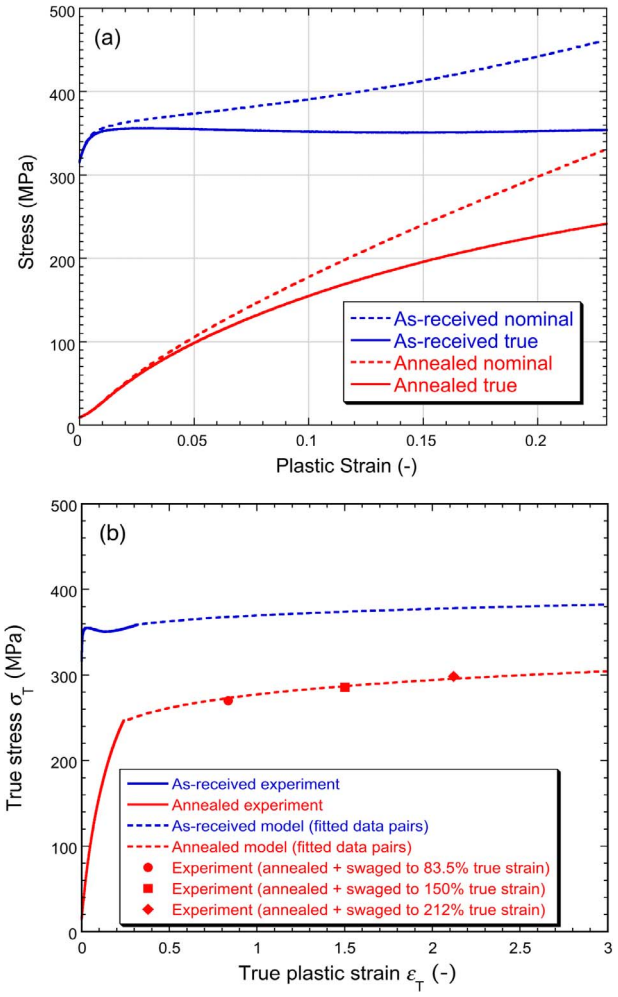

Fig. 5. Room temperature experimental and modelled quasi-static stress-strain plots for the two materials, showing (a) typical compression test data and (b) comparisons between modelled and measured plots of true stress against true strain, with the model representations shown up to high strain levels.

already happening for inferring quasi-static stress-strain relationships from load-displacement indentation data - see reference 26 - and something similar would be possible for evaluation of *C*.

4. Quasi-static plasticity

4.1. Stress-strain plots for ambient temperature

Data from typical compression tests (along the extrusion axis) with each material are shown in Fig. 5(a), plotted as both nominal and true values. The variation between tests was in general very small (< 1%). It can be seen that, as a true stress – true strain relationship, the as-received material (Fig. 5(a)) exhibits little or no strain (work) hardening. This is not unexpected, since the extrusion process probably left the material in a heavily cold-worked state. The annealed material, on the other hand, exhibits substantial strain hardening from the outset (Fig. 5(b)), with the relative change in flow stress during straining being much greater than that for the as-extruded material. This also is unsurprising for an annealed material. However, it does lead to a complication in the present context, in terms of representing the behaviour using Eq. (1). It should be noted that, while these uniaxial experiments often cannot be regarded as reliable beyond strains of the order of 20–25% (due to necking / failure in tension and barrelling in compression), strain levels well above this (perhaps of the order of at least 200%) can be generated during projectile impact, and are thus likely to be employed in the FEM model.

Under these circumstances, use of the equation with L-H parameter values fitted over the low strain regime leads to prediction of unrealistically high flow stresses at high strains. In practice, the flow stress is not expected to exceed that of the as-received material - they are, of course, basically the same material, apart from work-hardening effects. This behaviour therefore can't be represented realistically over a large strain range using the L-H equation. The solution adopted for the annealed material has therefore been to use sets of data pairs in the FEM model, conforming to the experimental outcome for low strains and constrained to conform to the yield stress values for the swaged samples (after well-defined degrees of prior cold work). This is illustrated in Fig. 5(b), which compares experimental data with extrapolated sets of data pairs, extending in both cases up to very high strains (~300%).

A comment is needed here with regard to the outcome of this procedure for the annealed material. It's clear that the curve does not have the expected shape around the transition between the directly measured range (up to about 20%) and the regime in which the flow stress has been obtained from the swaged samples. In practice, a smoother transition in gradient is expected. There are possible explanations for this discrepancy. For example, the swaging would have created more heating than the quasi-static loading, which may have promoted a degree of microstructural recovery during the process, hence softening the material somewhat. However, it would be difficult to compensate in any way for such effects and it seems simpler to just follow the described procedure, accepting that there are inevitably limits on the reliability of the (quasi-static) stress-strain curves.

The effect of anisotropy (due to crystallographic texture) is illustrated in Fig. 6, which compares the plots obtained by loading in axial or radial directions, for both materials. It can be seen that there is an effect, which is slightly more noticeable for the annealed material. Of course, the ballistic indentation was carried out only in the axial (extrusion) direction, but in that case the deformation is much more multiaxial than during compression testing, so that the overall response is expected to lie between the axial and radial extremes. If the objective were to obtain the quasi-static stress-strain curve from indentation data, and comparisons were being made with uniaxial outcomes, then this anisotropy would need to be taken into account. However, since the focus here is on the strain rate sensitivity, the exact shape on the base stress-strain curve is not expected to have a strong influence and so the data from axial testing were used in the modelling.

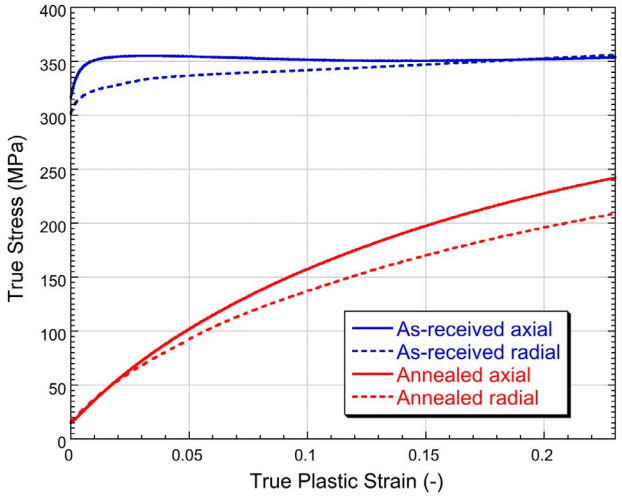

Fig. 6. Experimental uniaxial compression stress-strain plots for both materials, showing outcomes from loading in both axial and radial (transverse) directions.

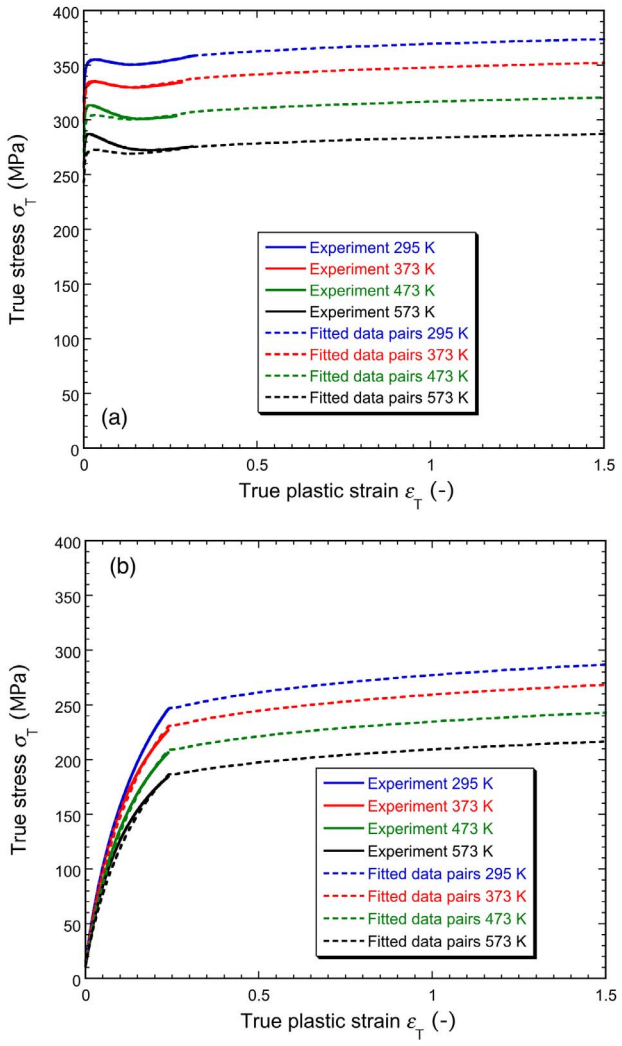

Fig. 7. Quasi-static true stress - true strain plots (experimental and modelled) over a range of temperature, for (a) as-received and (b) annealed materials. The value used for the temperature dependence parameter, m, is 1.09 in (a) and 1.05 in (b).

4.2. Stress-strain plots for elevated temperatures

True stress – true strain plots are shown in Fig. 7 for the four temperatures employed, together with best-fit modelled curves. In the temperature sensitivity part (second term in Eq. (1)), the melting temperature, T_m, was taken to be 1356 K and ambient temperature, T_0, to be 295 K. The dependence of the flow stress on temperature is reflected in the value of m (in Eq. (1)), with a low value giving a high sensitivity. It can be seen in the figure caption that the best-fit values of m were respectively 1.09 and 1.05 for as-received and annealed material.

Of course, there are difficulties associated with only being able to obtain experimental data over a strain range that is considerably smaller than the range likely to be experienced during an impact event, and also with the fact that this is purely an empirical curve-fitting exercise. Nevertheless, these modelled curves probably capture the quasi-static behaviour reasonably well. The as-received material does appear to undergo a small degree of initial strain softening (under axial loading), perhaps associated with liberation of some dislocations as straining starts (in an initially strain-hardened material).

5. Evaluation of the strain rate sensitivity parameter, C

5.1. Conditions during projectile penetration

The local conditions (fields of stress, strain, strain rate and temperature) after different degrees of penetration (δ/R values) naturally depend on both the incident velocity and the hardness (plasticity characteristics) of the sample. The present work covers two materials with very different hardness levels and, in each case, a range of impact velocities (covering a factor of about 3). It is helpful to at least be broadly aware of the nature of these fields in different cases, since this will give an indication of the ranges of strain, strain rate and temperature over which the stress-strain curves are expected to affect the response of the material.

Such predicted outcomes can, of course, only be obtained if a value is assumed for C. However, while this is unknown *a priori*, simply taking a value in the range that is broadly expected (eg. ~0.03) is acceptable for these purposes. A set of illustrative outcomes is shown in Fig. 8, which refers to the annealed material subjected to impact at 70 m s^{-1}, for 3 times after initial impact (the last corresponding to the point when the projectile has reached maximum penetration depth). The cumulative strains are shown in Fig. 8(a), where it can be seen that these peak at around 60%, with the region that has experienced fairly substantial strains (> ~30%) extending by the end of penetration to significant depths below the surface (~1 mm). The strain rates (Fig. 8(b)) peak at ~310^5 s^{-1}, but these occur only transiently in a small volume and most of the plastic deformation takes place at rates below 10^5 s^{-1}. Nevertheless, the figure does confirm that, even with this relatively low velocity, most of the plastic deformation takes place above 10^4 s^{-1}. This is related to Fig. 8(c), which shows that the flow stress at which much of the plastic deformation occurs is above the quasi-static value in the strain range concerned, which is ~300 MPa (at ambient temperature) - see Fig. 7(b). This confirms that strain rate hardening effects are significant (for this value of C). Finally, Fig. 8(d) confirms that the temperature rises are not very significant (less than 60 °C). Of course, this is a relatively low impact velocity (and copper is a very good conductor, assisting in dissipation of the heat evolved).

The influence of projectile velocity is illustrated by Fig. 9, in which the corresponding fields to those in Fig. 8 are presented for 200 m s^{-1}. As expected (since the incident kinetic energy is now greater by almost an order of magnitude), penetration is much deeper (almost to the "equator" of the ball) and the strains, strain rates, stresses and temperatures also reach higher values. However, some are increased more than others. It can be seen in Fig. 9(a) that the cumulative strains are raised considerably, reaching peaks of over 200% in places and exceeding 100% in relatively large volumes of material. Strain rates are also somewhat higher than for the lower velocity, peaking at nearly 10^6 s^{-1}, although again this is only for short periods in small volumes. The peak stress levels, on the other hand, are rather similar to those for the lower velocity impact and they drop off more quickly as the ball penetrates. This is due to the effect illustrated in Fig. 9(d), which shows that the temperature rises more quickly, and reaches relatively high values >150 °C) in a fairly large volume, bringing down the stress levels.

The material response for these two impact velocities will thus be sensitive to different parts of the family of stress-strain curves, with the main difference being that in the high velocity case there will be a greater sensitivity to the high strain regime (well beyond the limits of conventional uniaxial testing). For the as-received (work hardened) material, the behaviour will be different again, with strains being lower, but stresses being higher. Furthermore, the change in (quasi-static) flow stress as straining occurs will be less (and there is less uncertainty about the nature of the work-hardening). Of course, the two materials may have different strain rate sensitivities (values of C). There are no well-established ground rules for even approximate prediction of the value of C in different cases, although there might be an argument

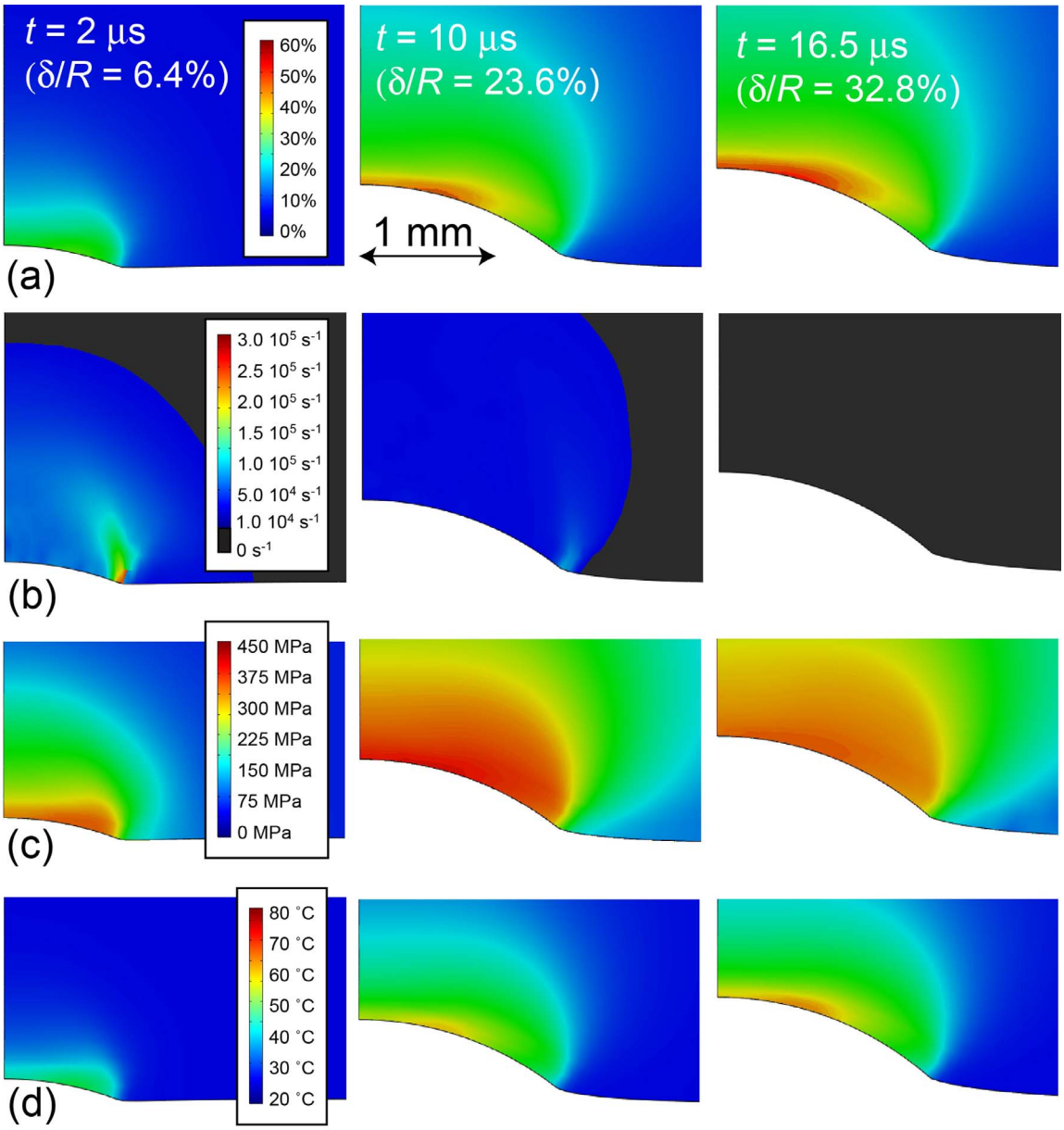

Fig. 8. Predicted FEM outcomes for the annealed material, with an incident projectile velocity of 70 m s^{-1} (assuming a strain rate sensitivity parameter, *C*, of 0.03), showing (a) total (von Mises) plastic strain, (b) strain rate, (c) deviatoric (von Mises) stress and (d) temperature, at 3 different times after initial impact.

for expecting softer materials (such as the annealed material here) to have higher values (since, when the quasi-static mobility of dislocations is high, larger changes in flow stress might be expected to result from imposing strain rates beyond levels that can be achieved by normal dislocation glide).

Finally, it may be noted that the peak strain rates are less important than the distribution of values that are effective locally while plastic deformation is occurring. This distribution is illustrated in Fig. 10(a) and (b), which provide data for both materials, with two different impact velocities. As expected, the average strain rate (weighted by the amount of plastic work done) is higher for the higher impact velocities, although the differences are not very great. (The average strain rates, weighted by plastic work, are 5.410^4 and 1.310^5 s^{-1} for (a) and 2.410^4 and 7.110^4 s^{-1} for (b)). Of course, a higher strain rate makes the material harder, tending to limit the amount of strain that occurs and hence reduce somewhat the amount of deformation occurring at such rates. On the other hand, with the initially softer material (Fig. 10(b)), while more deformation occurs, the strain rates tend to be lower than for the harder material. These plots demonstrate that the predominant strain rate range in these experiments is of the order of 10^4–10^5 s^{-1}, with values up to $\sim 10^6$ s^{-1} being generated in the harder material.

Finally, the significance of the frictional work is illustrated by Fig. 10(c), which compares (for the annealed material, with an impact velocity of 200 m s^{-1}) the strain rate distribution of the plastic work, obtained with the best fit value for μ of 0.1, with that in the absence of friction ($\mu = 0$). Of course, the plastic work done is lower when friction is included (due to some of the incident energy being absorbed by frictional sliding). It can be seen that this is a small, but not insignificant, fraction of the total work. It is also apparent that the frictional work is more significant in the higher strain rate regime, which is consistent with this taking place under conditions such that the normal stress at the interface (ie the contact pressure) is higher.

5.2. Evaluation of C for the as-received material

Illustrative comparisons for the as-received material are shown in

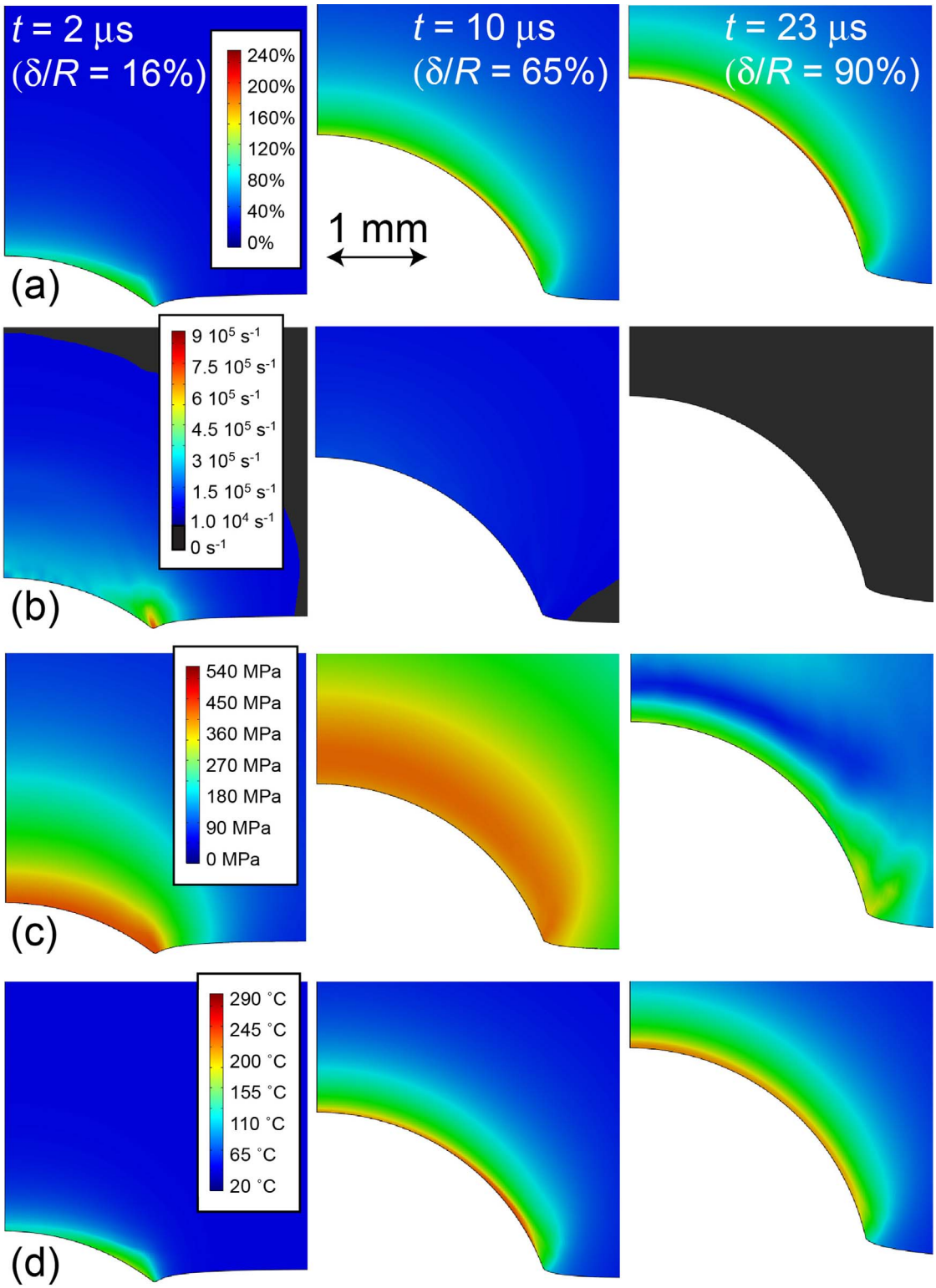

Fig. 9. Predicted FEM outcomes for the annealed material, with an incident projectile velocity of 200 m s^{-1} (assuming a strain rate sensitivity parameter, *C*, of 0.03), showing (a) total (von Mises) plastic strain, (b) strain rate, (c) deviatoric (von Mises) stress and (d) temperature, at 3 different times after initial impact.

Fig. 11 between model outcomes and experimental data, with 3 different incident velocities, in terms of projectile displacement histories and residual indent shapes. These predictions are for a particular value of *C* (0.016). It can be seen that, in both cases, the agreement is fairly good (*g* values around 0.8–0.9 in all cases). Such comparisons were made for a range of *C* values, with the goodness-of-fit parameter, *g*, being evaluated in each case. The outcome of this set of comparisons is summarised in Fig. 12, which shows plots of *g* as a function of *C*, for each type of comparison, and for each of the 3 impact velocities. While the outcome is not entirely consistent, optimum values of *C* are mostly around 0.016. It should be recognised that this procedure constitutes a comprehensive examination, not only of the value of *C*, but also of the reliability of the J-C formulation. The outcome does suggest that it is at least approximately valid, with, for this (work-hardened) material, the appropriate value of *C* apparently being $\sim 0.016 \pm 0.005$.

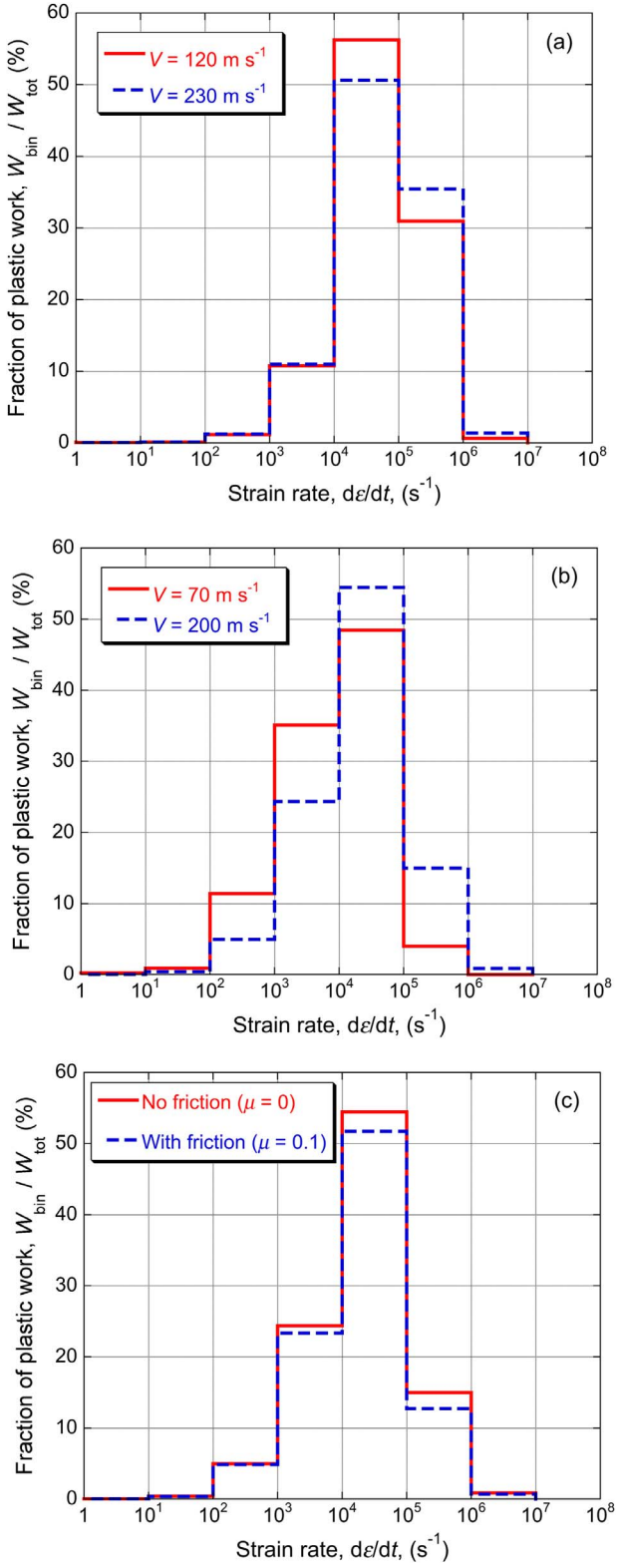

Fig. 10. Histograms of strain rate ranges within which plastic work was done ($C = 0.03$). Plots (a) and (b) relate to as-received and annealed materials, with two impact velocities and no friction, while plot (c), which is for the annealed material, with $V = 200\,\mathrm{m\,s^{-1}}$, shows the effect of friction.

5.3. Evaluation of C for the annealed material

Corresponding plots to Figs. 11 and 12, for the annealed material, are shown in Figs. 13 and 14. The comparisons in Fig. 13 are for

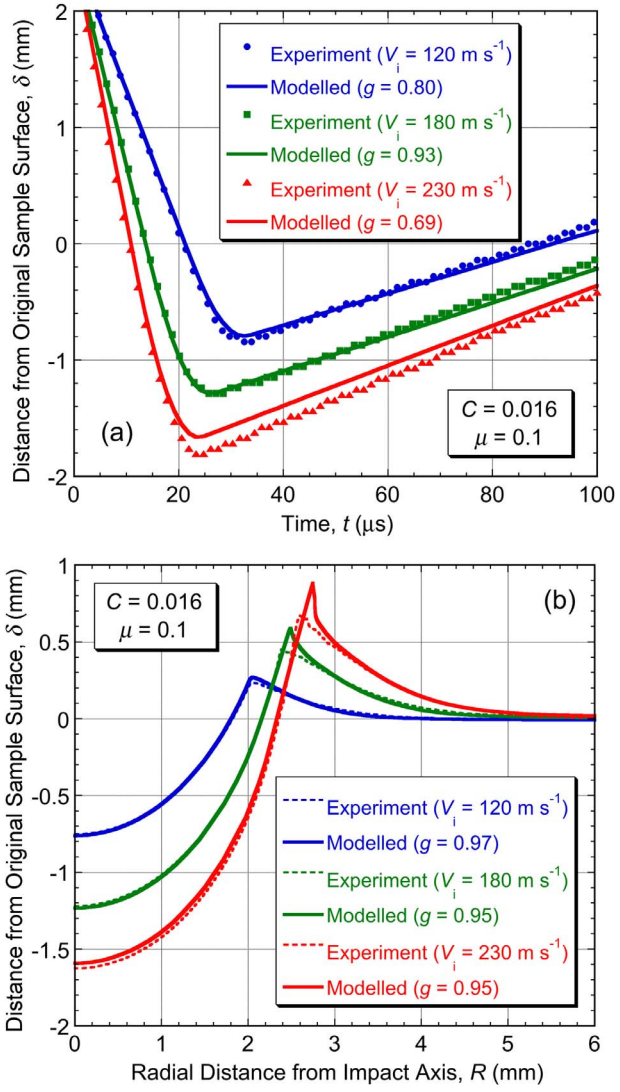

Fig. 11. Comparisons, for 3 different impact velocities, between model predictions (with $C = 0.016$ and $\mu = 0.1$) and experimental data, for the as-received material, showing (a) displacement histories (from high-speed photography) and (b) residual indent shapes (from profilometry). The level of agreement in each case is characterised by the values shown for the goodness-of-fit parameter, g.

$C = 0.030$. It can be seen that agreement is again quite good, with this value of C, for both high-speed photography and profilometry data. It is also clear from the $g(C)$ plots in Fig. 14 that a higher value of C than for the as-received material gives the best agreement for the annealed samples. Again, the agreement is not perfect. In particular, the plots for the $V = 70\,\mathrm{m\ s^{-1}}$ case appear to be a little inconsistent, apparently indicating a best-fit C value above 0.04 for the displacement data and below 0.02 for the indent shape data. This could be at least partly attributable to the fact that the strain rates were relatively low in this case, which is likely to introduce errors into the inferred value of C. Taken overall, the results for the annealed material indicate that the most appropriate value of C is about 0.030 ± 0.010.

5.4. Reliability of the inferred values of C

While it is difficult to compare these values with anything in a systematic way, they are of a similar magnitude to those reported in a number of previous publications [9,17–21] (for a range of metals). Furthermore, that the softer material should be more susceptible to strain rate hardening (higher value of C) than the harder material (when, apart from the degree of prior work hardening, they are

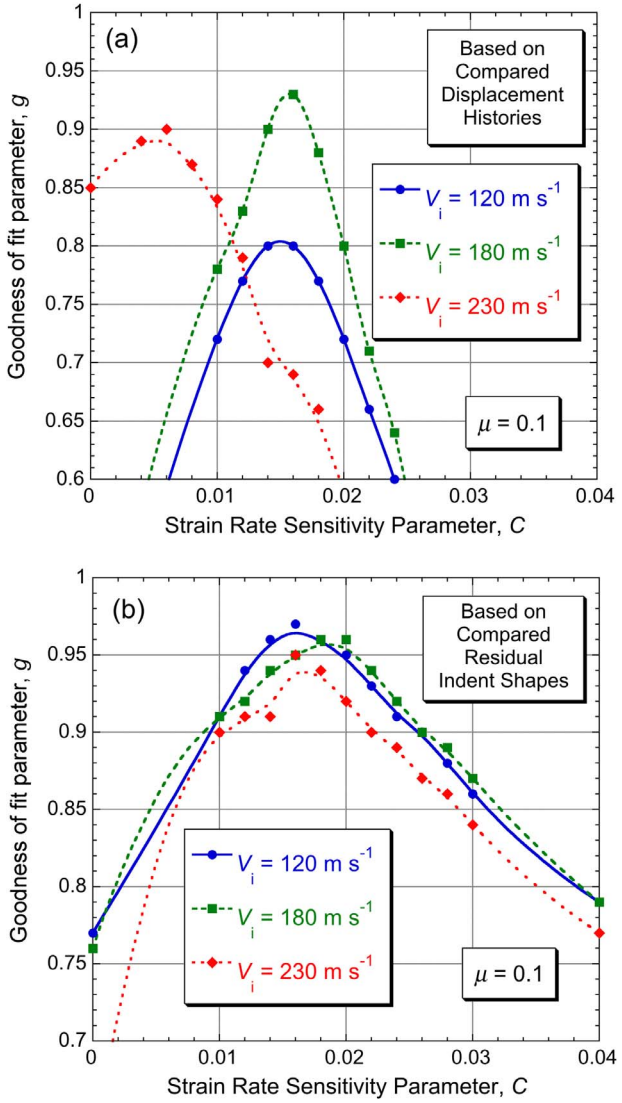

Fig. 12. Plots, for 3 different impact velocities, of $g(C)$, for the as-received material, based on (a) projectile displacement histories and (b) residual indent shapes.

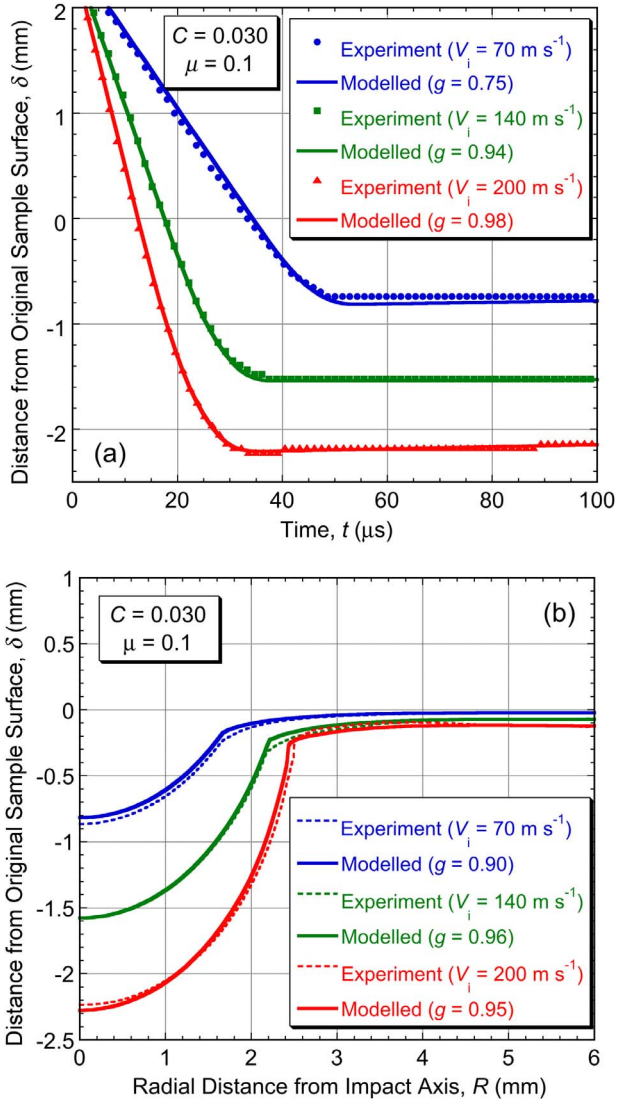

Fig. 13. Comparisons, for 3 different impact velocities, between model predictions (with C = 0.030 and μ = 0.1) and experimental data, for the annealed material, showing (a) displacement histories (from high-speed photography) and (b) residual indent shapes (from profilometry). The level of agreement in each case is characterised by the values shown for the goodness-of-fit parameter, g.

essentially the same material) certainly appears to be plausible: there is clearly more scope for relatively greater hardening with softer materials and it thus seems likely that the effect of an increased strain rate would be more noticeable (although this is not a rigorous argument). In fact, the data presented here are more comprehensive than those of earlier studies, both in terms of the spatial and temporal variations in local strain rate being fully incorporated into the modelling and because two independent sets of experimental measurements have been obtained in each case. The fact that, in general, both types of measurement point to similar values of C in each case does allow increased confidence in their reliability.

In detail, there are certainly some discrepancies, notably in terms of the results for the softer material, for which the outcome with the lower impact velocity (strain rates) appears a little inconsistent with those dominated by higher strain rates. It's clear that the J-C formulation is simplistic, with complete decoupling of the base shape of the stress-strain curve, the softening effect of raising the temperature and the hardening effect of raising the strain rate. From a mechanistic (microstructural) point of view, it is the mobility of dislocations that is the key factor (with deformation twinning being rather unlikely in these two materials), and, while this will be enhanced by high temperature and reduced by imposing a high strain rate, it's quite likely that there would be some kind of inter-dependence between the two effects. Furthermore, studies [27,28] aimed at exploring dislocation dynamics over a range of (high) strain rates have indicated that there is often a transition in the rate-determining process as the strain rate is increased (for example, from the rate of motion of existing dislocations to the rate of nucleation of new ones at a shock front). It is therefore not unreasonable to expect that the apparent strain rate sensitivity would be different in two experiments in which the strain was imposed at substantially different average strain rates (with different degrees of heating). However, there may be a danger of over-analysing these results, which do, in general, confirm that the J-C formulation appears to provide a broadly reliable description of the strain rate sensitivity, and also that the proposed methodology allows this sensitivity to be quantified in approximate terms. Of course, the methodology could also be used to check on the reliability of alternative formulations.

6. Conclusions

The following conclusions can be drawn from this work:

(a) A novel procedure has been developed for experimental evaluation

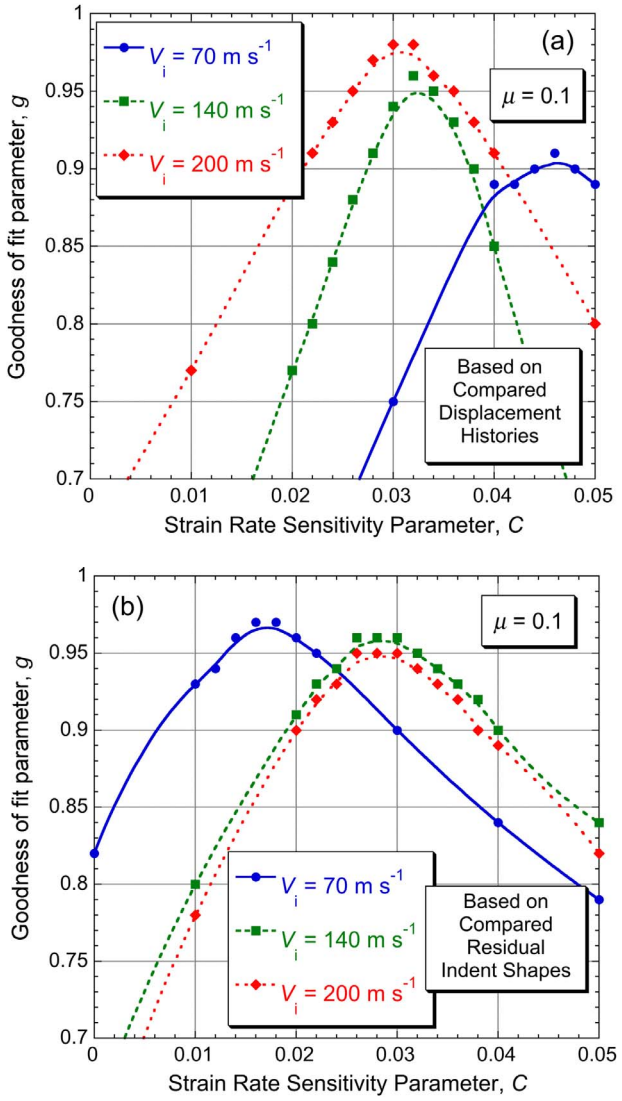

Fig. 14. Plots, for 3 different impact velocities, of $g(C)$, for the annealed material, based on (a) projectile displacement histories and (b) residual indent shapes.

of the strain rate sensitivity parameter, C, in the Johnson–Cook equation (which would also be applicable to other formulations). It involves impact of the sample by a hard spherical projectile, followed by monitoring of its penetration and rebound by high-speed photography and/or profilometry of the residual indent shape. Iterative FEM simulation is then carried out, using trial values for C, with quantification of the level of agreement between predicted and measured outcomes. Input requirements for the model include data characterising the quasi-static plasticity behaviour of the material (over a range of temperature) and also the effect of interfacial friction (which apparently has a small, but detectable, influence).

(b) This procedure has been carried out on two different materials, in the form of as-received (work-hardened) and annealed copper. In both cases, three different impact velocities were used (~50–250 m s^{-1}), with both high-speed photography and residual indent profilometry being employed. Good levels of agreement were obtained (using best-fit values of C), over the range of velocity employed, for both types of experimental data. The strain rates operative during the plastic deformation were predominantly of the order of 10^4–10^6 s^{-1}.

(c) The values obtained for C were 0.016 ± 0.005 for the harder (as-received) material and 0.030 ± 0.010 for the softer (annealed) material. Using these values, the level of agreement observed between predicted and observed experimental outcomes is good, with goodness-of-fit parameter values mostly around 90–95%, allowing a reasonable level of confidence to be placed in both the broad reliability of the Johnson–Cook formulation and the accuracy of the inferred values of C.

(d) The procedure employed, while involving iterative FEM modelling runs, is one that is amenable to automated convergence. User-friendly software packages for its implementation, requiring no FEM expertise or resources, are likely to become available in the near future.

Acknowledgements

This work has been supported by EPSRC (grant RG62695) and also by AWE, as part of an ongoing collaboration aimed at the development of robust and user-friendly tools for the extraction of mechanical property characteristics from instrumented indentation data. The authors are particularly grateful to Dr. G Aldrich–Smith and Dr. N Park, of AWE, for extensive discussions and interactions.

In compliance with current EPSRC requirements, input data for the modelling described in this paper, including meshing and boundary condition specifications, are available at the following URL: www.ccg.msm.cam.ac.uk/publications/resources. These files can be downloaded and used in FEM models.

Appendices

Appendix A. Nomenclature listing for the symbols used in the paper

Symbol	Meaning	Units
c	Heat capacity	Jm^{-3}K^{-1}
C	(Johnson-Cook) strain rate hardening parameter	–
E	Young's modulus	Pa
f	Function used in the operation of strain rate binning	–
g	Goodness-of-fit parameter	–
i	Counter for increments of time or radial location in g-screening	–
j	Counter for number of FEM volume elements in sample	–
k	Counter for increments of time during FEM modelling	–
K	Strain hardening coefficient	Pa
m	Temperature sensitivity exponent	–
M	Total number of volume elements in sample	–
n	Strain hardening exponent	–
N	Number of comparisons between modelled & measured δ values	–

R	Radius of (spherical) projectile	m
S	Total number of time steps during FEM simulation	–
t	Time	s
T	Temperature	K
T_0	Reference (ambient) temperature	K
T_m	Melting temperature	K
v	Volume	m^3
V	Impact velocity	$m\ s^{-1}$
W	Plastic work	J
δ	Displacement (relative to sample surface)	m
$\Delta\delta_i$	Difference in displacement (between model and experiment)	m
δ_{av}	Average displacement (over comparison range)	m
ε_p	Equivalent (plastic) strain	–
$d\varepsilon_p/dt$	Strain rate	s^{-1}
$(d\varepsilon_p/dt)_0$	Reference (quasi-static) strain rate	s^{-1}
K	Thermal conductivity	$W\ m^{-1}\ K^{-1}$
ν	Poisson ratio	–
σ	(Von Mises) stress	Pa
σ_Y	(Uniaxial) yield stress	Pa

Supplementary material

Supplementary material associated with this article can be found, in the online version, at 10.1016/j.ijimpeng.2017.10.012.

References

[1] Umbrello D, M'Saoubi R, Outeiro JC. The influence of Johnson–Cook material constants on finite element simulation of machining of AISI 316 L steel. Int J Mach Tools Manuf 2007;47(3–4):462–70.
[2] Johnson GR, Cook WH. A constitutive model and data for metals subjected to large strains, high strain rates and high temperatures. Proce. 7th Int. Symp. on Ballistics 1983;21:541–7.
[3] Molinari A, Ravichandran G. Fundamental structure of steady plastic shock waves in metals. J Appl Phys 2004;95(4):1718–32.
[4] Rule WK, Jones SE. A revised form for the Johnson–Cook strength model. Int J Impact Eng 1998;21(8):609–24.
[5] Lin YC, Chen XM, Liu G. A modified Johnson-Cook model for tensile behaviors of typical high-strength alloy steel. Mater Sci Eng A-Struct Mater Prop Microstruct Process 2010;527(26):6980–6.
[6] He A, Xie GL, Zhang HL, Wang XT. A comparative study on Johnson–Cook, modified Johnson–Cook and Arrhenius-type constitutive models to predict the high temperature flow stress in 20CrMo alloy steel. Mater Des 2013;52:677–85.
[7] Manes A, Peroni L, Scapin M, Giglio M. Analysis of strain rate behavior of an A1 6061 T6 alloy. In: Guagliano M, Vergani L, editors. Amsterdam: Elsevier Science Bv; 2011. p. 3477–82.
[8] Holmen JK, Hopperstad OS, Borvik T. Influence of yield-surface shape in simulation of ballistic impact. Int J Impact Eng 2017;108:136–46.
[9] Jordan JL, Siviour CR, Sunny G, Bramlette C, Spowart JE. Strain rate-dependant mechanical properties of OFHC copper. J Mater Sci 2013;48(20):7134–41.
[10] Bertholf LD, Karnes CH. 2-dimensional analysis of split Hopkinson pressure bar system. J Mech Phys Solids 1975;23(1):1–19.
[11] Chen WNW, Song B. Split Hopkinson (Kolsky) bar: design, testing and applications. Split Hopkinson. New York: Springer; 2011. 1–+.
[12] Gama BA, Lopatnikov SL, Gillespie Jr JW. Hopkinson bar experimental technique: a critical review. Appl Mech Rev 2004;57:223.
[13] Prabowo DA, Kariem MA, Gunawan L. The effect of specimen dimension on the results of the Split-Hopkinson tension bar testing. In: Gupta N K, Iqbal M A, editors. Plasticity and impact mechanics. Amsterdam: Elsevier Science Bv; 2017. p. 608–14.
[14] Maudlin PJ, Bingert JF, House JW, Chen SR. On the modeling of the Taylor cylinder impact test for orthotropic textured materials: experiments and simulations. Int J Plastic 1999;15(2):139–66.
[15] Maudlin PJ, Gray GT, Cady CM, Kaschner GC. High-rate material modelling and validation using the Taylor cylinder impact test. Philos Trans Royal Soc A-Math Phys Eng Sci 1999;357(1756)):1707–29.
[16] Lopatnikov SL, Gama BA, Haque MJ, Krauthauser C, Gillespie JW, Guden M, et al. Dynamics of metal foam deformation during Taylor cylinder-Hopkinson bar impact experiment. Compos Struct 2003;61(1–2):61–71.
[17] Noh HG, An WJ, Park HG, Kang BS, Kim J. Verification of dynamic flow stress obtained using split Hopkinson pressure test bar with high-speed forming process. Int J Adv Manuf Technol 2017;91(1–4):629–40.
[18] Mylonas GI, Labeas GN. Mechanical characterisation of aluminium alloy 7449-T7651 at high strain rates and elevated temperatures using split hopkinson bar testing. Exp Tech 2014;38(2):26–34.
[19] Sedighi M, Khandaei M, Shokrollahi H. An approach in parametric identification of high strain rate constitutive model using Hopkinson pressure bar test results. Mater Sci Eng A-Struct Mater Prop Microstruct Process 2010;527(15):3521–8.
[20] Sasso M, Newaz G, Amodio D. Material characterization at high strain rate by Hopkinson bar tests and finite element optimization. Mater Sci Eng A-Struct Mater Prop Microstruct Process 2008;487(1–2):289–300.
[21] Mishra A, Martin M, Thadhani NN, Kad BK, Kenik EA, Meyers MA. High-strain-rate response of ultra-fine-grained copper. Acta Materialia 2008;56(12):2770–83.
[22] Gavrus A, Le Baron JP, Caestecker P, Ragneau E. Investigation of high speed behaviour of ductile materials by computer simulation and Hopkinson experimental test. In: Miannay D, Costa P, Francois D, Pineau A, editors. Advances in mechanical behaviour, plasticity and damage, vols 1 and 2, proceedings. Amsterdam: Elsevier Science Bv.; 2000. p. 535–40.
[23] Andrews E, Giannakopoulos AE, Plisson E, Suresh S. Analysis of the impact of a sharp indenter. Int J Solids Struct 2002;39:281–95.
[24] Lu J, Suresh S, Ravichandran G. Dynamic indentation for determining the strain rate sensitivity of metals. J Mech Phys Solids 2003;51:1923–38.
[25] Skordaris G, Bouzakis KD, Charalampous P. A dynamic FEM simulation of the nano-impact test on mono- or multi-layered PVD coatings considering their graded strength properties determined by experimental-analytical procedures. Surf Coat Technol 2015;265:53–61.
[26] Dean J, Clyne TW. Extraction of plasticity parameters from a single test using a spherical indenter and FEM modelling. Mech Mater 2017;105:112–22.
[27] Zerilli FJ, Armstrong RW. The effect of dislocation drag on the stress-strain behavior of FCC metals. Acta Metallur Et Mater 1992;40(8):1803–8.
[28] Armstrong RW, Arnold W, Zerilli FJ. Dislocation mechanics of shock-induced plasticity. Metallur Mater Trans A-Phys Metallur Mater Sci 2007;38A(11):2605–10.